

A MIXED ASSUMED STRAIN FINITE ELEMENT FORMULATION FOR VARIATIONAL-BASED ENERGY-MOMENTUM TIME INTEGRATIONS IN THERMODYNAMICS OF FIBER-REINFORCED CONTINUA

MICHAEL GROSS¹ AND JULIAN DIETZSCH²

¹ Technische Universität Chemnitz, Professorship of applied mechanics and dynamics,
Reichenhainer Straße 70, D-09107 Chemnitz, email: michael.gross@mb.tu-chemnitz.de

² email: julian.dietzsch@mb.tu-chemnitz.de

Key words: Fiber-reinforced continuum, anisotropy, energy-momentum time integration, higher-order finite elements in space and time, multi-field principle of virtual power.

Abstract. In this paper, we present a new higher-order accurate energy-momentum time integration of fiber-reinforced thermo-viscoelastic continua. The energy-momentum schemes are derived from a multi-field principle of virtual power (cp. Reference [13]). We consider thermal volume expansion of a visco-elastic matrix material and thermal expansion of unidirectional fibers, as well as transversely-isotropic heat conduction due to Reference [14]. Therefore, in addition to the linear momentum and the deformation, the entropy and the temperature are approximated independently in space and time. The used multi-field principle of virtual power also introduces the strains and stresses of the matrix as well as the fiber strains and stresses as independent variables. As we consider an isochoric-volumetric decoupling of the free energy function of the matrix material, the volumetric strain and stress fields are approximated independently by spatial and temporal finite elements. In this way, the third and fourth tensor invariant of the right-Cauchy Green tensor and the structural tensor of the considered transversely-isotropic material are independent fields and discretized independently in space and time together with their associated dual variables. We show a numerical example with transient Dirichlet and Neumann boundary conditions, which compare these space-time approximations regarding locking behaviour in the matrix (volumetric locking) and the fibers (line locking).

1 INTRODUCTION

Locking-free finite elements and energy-momentum schemes are two of the best-known algorithmic improvements of dynamic finite element methods. Both are developed since the middle of the eighties of the last century, but usually independently from each other. Therefore, a smart interface between both methods is rarely a goal of the development. In this paper, we present such a smart interface, namely the Hu-Washizu procedure applied

to the principle of *virtual power*. By applying this variational principle to a dynamical problem, we show a new alternative to the Simo-Taylor-Pister functional

$$\Pi_{\text{STP}}(\boldsymbol{\varphi}, \tilde{J}, p) := \int_{\mathcal{B}_0} \Psi^{\text{iso}}(\tilde{\mathbf{C}}(\boldsymbol{\varphi})) \, dV + \int_{\mathcal{B}_0} \Psi^{\text{vol}}(\tilde{J}) \, dV - \int_{\mathcal{B}_0} p \left[\tilde{J} - \det \mathbf{F}(\boldsymbol{\varphi}) \right] \, dV + \Pi^{\text{ext}}(\boldsymbol{\varphi}) \quad (1)$$

which is based on an isochoric free energy function Ψ^{iso} depending directly on the unimodular part $\tilde{\mathbf{C}} := (\det \mathbf{C})^{-\frac{1}{n_{\text{dim}}}} \mathbf{C}$ of the right Cauchy-Green tensor $\mathbf{C} := \mathbf{F}^T \mathbf{F}$. The tensor $\mathbf{F} := \partial \boldsymbol{\varphi} / \partial \mathbf{X}$, with $\mathbf{X} \in \mathcal{B}_0$, designates the deformation gradient, and $\boldsymbol{\varphi} : \mathcal{B}_0 \rightarrow \mathcal{B}_t$ denotes the deformation mapping between the initial configuration \mathcal{B}_0 and the current configuration \mathcal{B}_t . Recall that, due to the Hu-Washizu procedure, Ψ^{vol} depends on the independent dilatation \tilde{J} of the body. The independent pressure p indicates the Lagrange multiplier, which enforces the condition $\tilde{J} = \det \mathbf{F}$. $\Pi^{\text{ext}}(\boldsymbol{\varphi})$ denotes the potential energy of external loads (compare References [1, 2, 3]). In the standard way, using the principle of virtual work, Π_{STP} has to fulfill the condition

$$\delta \Pi_{\text{STP}} \equiv D_1 \Pi_{\text{STP}}(\boldsymbol{\varphi}, \tilde{J}, p)[\delta \boldsymbol{\varphi}] + D_2 \Pi_{\text{STP}}(\boldsymbol{\varphi}, \tilde{J}, p)[\delta \tilde{J}] + D_3 \Pi_{\text{STP}}(\boldsymbol{\varphi}, \tilde{J}, p)[\delta p] = 0 \quad (2)$$

where $D_i f(x_1, \dots, x_i, \dots, x_n)[\delta x_i]$ denotes the functional derivative of $f(x_1, \dots, x_i, \dots, x_n)$ in direction of the variation field δx_i . Hence, we obtain the Euler-Lagrange equations

$$\tilde{J} = \det \mathbf{F}(\boldsymbol{\varphi}) \quad p = \frac{\partial \Psi^{\text{vol}}(\tilde{J})}{\partial \tilde{J}} \quad (3)$$

which define the dilatation \tilde{J}_t and the pressure p_t at time t of a motion directly and indirectly, respectively, *only* via the corresponding deformation mapping $\boldsymbol{\varphi}_t$ (compare Reference [4]). Therefore, the mixed variables \tilde{J} and p are not *directly* related with continuous time curves $t \mapsto \tilde{J}(t, \mathcal{B}_0)$ and $t \mapsto p(t, \mathcal{B}_0)$, respectively. In contrast, any configuration $\boldsymbol{\varphi}_t(\mathcal{B}_0)$ is directly related with its previous configuration $\boldsymbol{\varphi}_{t-dt}(\mathcal{B}_0)$, because the equation of motion includes the partial time derivative of the material velocity $\mathbf{v} := \partial \boldsymbol{\varphi} / \partial t \equiv \dot{\boldsymbol{\varphi}}$. Therefore, we require initial positions and initial velocities for defining a unique motion $t \mapsto \boldsymbol{\varphi}(t, \mathcal{B}_0)$ of the body. However, in Reference [5], it is shown that a continuous time curve $t \mapsto \tilde{\mathbf{C}}(t, \mathcal{B}_0)$ of the right Cauchy-Green tensor as mixed field $\tilde{\mathbf{C}}$ follows from a variational principle automatically, if the principle of virtual power is used. Therefore, in this paper, we combine the Hu-Washizu procedure with the *principle of virtual power*.

By using the resulting mixed variational principle, we avoid locking in a spatial finite element discretization of non-isothermal inelastic fiber-reinforced materials, and obtain a family of robust higher-order accurate energy-momentum schemes. We consider volumetric locking in the matrix material and line locking in the fibers of an unidirectional fiber-reinforced continuum. We also show that this reduction of locking in the energy-momentum schemes leads to an increase of the maximum time step size. Therefore, the efficiency of the time integration is improved in the sense that less CPU time is required. This could be achieved by using an iteration-count dynamic time step size control, wherein

the iteration number of the applied global Newton-Raphson scheme is the target function. As numerical example, we consider a transient loading of a thin-walled fiber-reinforced structure, simulated by mechanical and thermal Dirichlet and Neumann boundaries.

2 NUMERICAL EXAMPLE

After discretizing the weak forms resulting from the principle of virtual power by finite elements in space and time, we obtain an energy-momentum scheme with the following features: Firstly, the discrete kinetic, potential and thermal energy balance is preserved, leading to the preservation of the discrete total energy balance. Secondly, the discrete total linear, angular and entropy balance is preserved, which leads to the discrete Lyapunov function balance. On the other hand, we discretize the mechanical, thermal and viscous residuals with different time scales, i.e. with different temporal shape functions of degree k^{mec} , k^{the} and k^{vis} , respectively. Further, we determine the Dirichlet reactions in the post-processing (compare Reference [6]), and combine the scheme with an iteration-count dynamic time step size control. This scheme render the following numerical results:

In Reference [7], we show an investigation of variational-based higher-order energy-momentum schemes for each permutation $(k^{\text{mec}}, k^{\text{the}}, k^{\text{vis}})$ of a temporal approximation, $k = 1, 2, 3$, by using the mentioned iteration-count dynamic time step size control. We found out that the higher-order energy-momentum schemes allow larger time steps with increasing k^{mec} , k^{the} and k^{vis} , but the most efficient scheme is the combination $(k^{\text{mec}}, k^{\text{the}}, k^{\text{vis}}) = (1, 2, 1)$. Here, we obtain the best compromise between a small number of time steps and a short total CPU time. Therefore, in this paper, we restrict ourselves to present simulations using this 121-scheme with different strain-stress approximations.

We compare the D1 approximation in Reference [7], where the strain and the stress are considered locally at spatial quadrature points, with the new strain-stress space approximation presented in this paper. We use the notation D1F0 for the 121-scheme with the \tilde{C}_F - S_F space approximation in the fibers, and a volumetric part of the free energy approximated by \tilde{C} (no volumetric fields \tilde{C}_V and S_V are introduced). Further, we apply the notation D1V0F0 for the 121-scheme with a \tilde{C}_V - S_V as well as a \tilde{C}_F - S_F space approximation. In these indicators, D means ‘displacement’, V means ‘volumetric’, F means ‘fiber’, and the numbers designate the degree of the spatial shape functions, analogous to the well-known indicator $Q1P0$ for the assumed pressure approximation (see Reference [6]). Therefore, D1V0F0 denotes a 8-node hexahedral element in the displacements and one node in the space approximation of volumetric and fiber strain and stress, respectively. We also investigate the D2V1F1 space approximation with a 20-node hexahedral element in the displacements and the 8-node hexahedral element in the volumetric and fiber strain and stress, respectively. The resulting systems of linear equations in the Newton-Raphson schemes and the strain-stress condensation are solved according to Reference [8], and the spatial meshing of the presented numerical example is provided by Reference [9].

As locking is especially pronounced for thin-walled structures (see Reference [10]), we simulate a spherical shell with a slit under mechanical und thermal loads. The geometry of the shell is depicted in Figure 1. The outer radius of the shell is given by $r_{\text{outer}} = 50$ and the wall thickness reads $d_{\text{wall}} = 2.5$. By considering the initial conditions

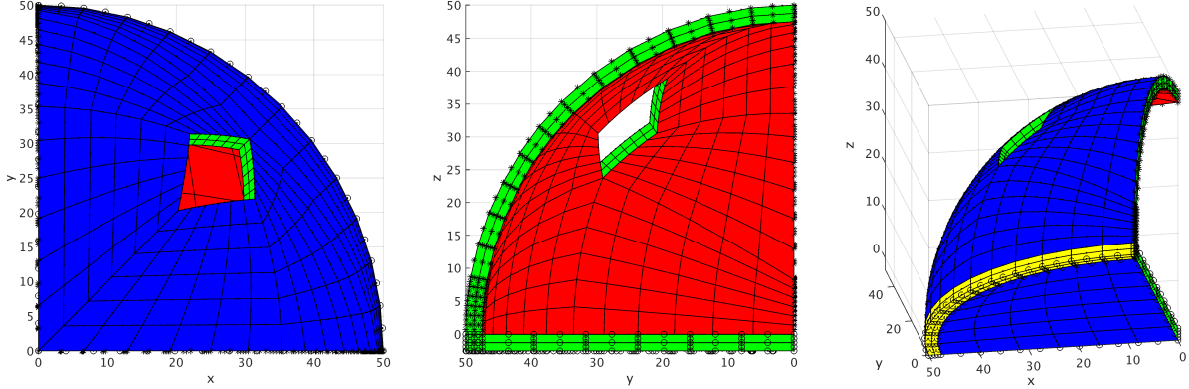


Figure 1: Boundary Status Monitor: Boundary conditions of the fiber-reinforced spherical shell with a slit indicated by colours and markers. Yellow patches designate the thermal Dirichlet boundary $\partial_{\hat{\Theta}}\mathcal{B}_0$ (bottom) and blue patches designate the thermal Dirichlet boundary $\partial_{\Theta}\mathcal{B}_0$. Red and green patches designate the thermal Neumann boundary $\partial_Q\mathcal{B}_0$. Circular markers designate the mechanical Dirichlet boundary $\partial_{\varphi}\mathcal{B}_0$, where star markers designate the hydrodynamic pressure boundary $\partial_T\mathcal{B}_0$.

$$\varphi_0^A = \mathbf{X}^A \quad \mathbf{v}_0^A = \mathbf{0} \quad \Theta_0^A = \Theta_{\infty} + 10 \quad (4)$$

with the ambient temperature $\Theta_{\infty} = 298.15$, the considered motion only arises from the applied transient loads subject to further boundary conditions. We consider on the narrow sides of the shell (the green patches with star markers in Figure 1) a transient pressure

$$f_p(t) := \hat{p} |\sin(\omega_{\text{load},p} t)| \quad (5)$$

as follower load (mechanical Neumann boundary $\partial_T\mathcal{B}_0$) in the line of Reference [2, 11]. Additionally, we prescribe on the yellow patches nodal temperatures $\Theta^A = \hat{\Theta} f(t)$ (thermal Dirichlet boundary $\partial_{\hat{\Theta}}\mathcal{B}_0$) with the time profile

$$f(t) = \begin{cases} (1.0 f_L(t))^2 \quad \forall T_{\text{load}}(0.0 + c_{\text{load}}) < t \leq T_{\text{load}}(0.2 + c_{\text{load}}) \\ (1.2 f_L(t))^2 \quad \forall T_{\text{load}}(0.2 + c_{\text{load}}) < t \leq T_{\text{load}}(0.4 + c_{\text{load}}) \\ (1.4 f_L(t))^2 \quad \forall T_{\text{load}}(0.4 + c_{\text{load}}) < t \leq T_{\text{load}}(0.6 + c_{\text{load}}) \\ (1.2 f_L(t))^2 \quad \forall T_{\text{load}}(0.6 + c_{\text{load}}) < t \leq T_{\text{load}}(0.8 + c_{\text{load}}) \\ (1.0 f_L(t))^2 \quad \forall T_{\text{load}}(0.8 + c_{\text{load}}) < t \leq T_{\text{load}}(1.0 + c_{\text{load}}) \end{cases} \quad (6)$$

where $f_L(t) := \sin(\omega_{\text{load}} t)$ denotes a load function and $c_{\text{load}} = 0, 1, \dots, \infty$ a load cycle counter. The amplitude \hat{p} in Eq. (5), the amplitude $\hat{\Theta}$ as well as the angular frequencies $\omega_{\text{load},p}$, ω_{load} and the load time duration T_{load} are stated in Table 1. Circular markers on the yellow and green patches denote the mechanical Dirichlet boundary $\partial_{\varphi}\mathcal{B}_0$ of the shell. Where on the yellow patches the z -dofs are fixed, on the green patches the x - or y -dofs are prescribed, respectively. The blue patches indicate the thermal Dirichlet boundary $\partial_{\Theta}\mathcal{B}_0$ with a constant boundary temperature Θ_{∞} . Green and red patches formally indicate the thermal Neumann boundary $\partial_Q\mathcal{B}_0$, too. We prescribe a vanishing heat flux $\bar{Q} = 0$, such that the shell is here thermally insulated. We also consider standard gravity in $\mathbf{e}_g = -\mathbf{e}_z$ direction. The direction vector field $\mathbf{a}_0(\mathbf{X}) = \mathbf{e}_z \times \mathbf{X} / \|\mathbf{X}\|$ of the fibers in the reference configuration \mathcal{B}_0 is depicted in Figure 2.

Table 1: Simulation parameters and boundary conditions of the spherical shell with a slit.

Initial conditions	
Initial velocity:	$\mathbf{v}_0^A = \mathbf{0}$
Initial temperature:	$\Theta_0^A = \Theta_\infty + 10 = 308.15$
Boundary conditions	
Green patches in xz-plane:	y -dof fixed
Green patches in yz-plane:	x -dof fixed
Yellow patches in xy-plane (with circular markers):	z -dof fixed
Yellow patches:	$\Theta^A = \hat{\Theta} f(t)$
Blue patches:	$\Theta^A = \Theta_\infty$
Green and red patches:	$\bar{Q} = 0$ (thermal insulation)
Dirichlet loads	
Temperature profile: (yellow patches)	$f(t)$ with $\hat{\Theta} = 10$ $T_{\text{load}} = 2.0, \omega_{\text{load}} = 10\pi$
Neumann loads	
Pressure load: (green patches with star marker)	$f_p(t)$ with $\hat{p} = 1 \cdot 10^5$ $T_{\text{load,p}} = 2.0, \omega_{\text{load,p}} = 10\pi$
Volume loads	
Standard gravity	$g = 9.81$ with $\mathbf{e}_g = -\mathbf{e}_z$

2.1 The simulated motion - dynamic bending and buckling of a shell

In this section, we present the simulation results generated by the D2V1F1 space approximation in the time interval $[0, 2.0]$ as reference solution with 552 hexahedral 20-node/8-node elements. By means of this reference solution, we introduce the reader in the simulated motion.

In Figure 3, we show by means of the motion status monitor snapshots of the motion coloured by different physical fields. The top plot on the left monitors the volumetric stress field S_V over the body at time $t_n = 0.4$. Here, we recognize the stressed narrow sides of the shell, but also the highly stressed region below the slit. This is the result of the bending of the shell (compare the lowered upper tip at about $\mathbf{x}_{t_n} \approx 46 \mathbf{e}_z$). Where less bending deformations are generated, we obtain a low volumetric stress (see the light blue coloured patches of the tips). In the top right plot, we show the current configuration at time $t_n = 0.8$ coloured by the fiber stress field S_F . Here, we realize that also the fibers are stressed by the bending. Therefore, the fiber strain in the bottom of the shell is also increased. The bottom left plot shows the shell at time $t_n = 1.0$, where the temperature profile in Eq. (6) possesses its maximum value. Therefore, the thermal Dirichlet boundary $\partial_{\hat{\Theta}} \mathcal{B}_0$ (yellow patches in Figure 1) are dark red coloured, which means that here the highest nodal temperatures arise. The region below the slit is dark blue coloured (low

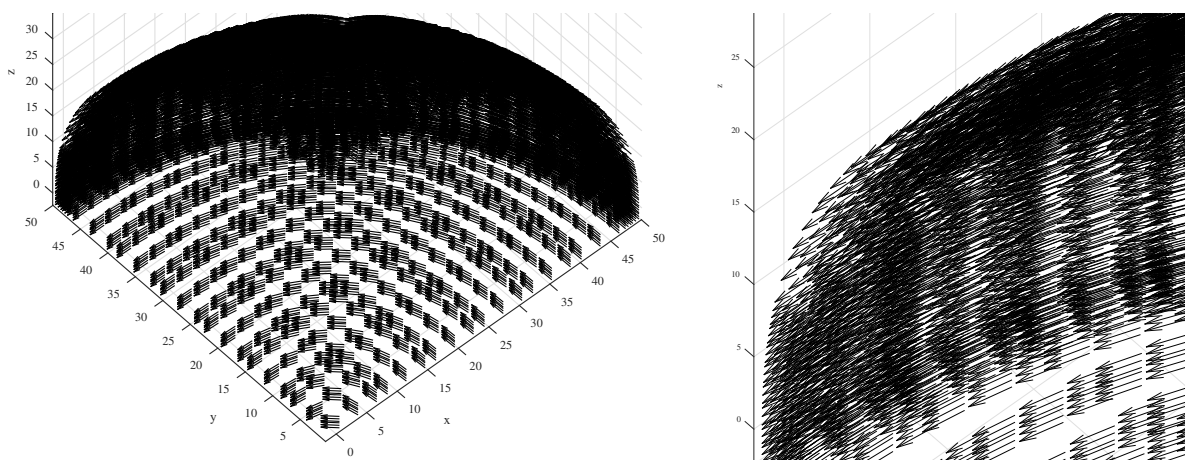


Figure 2: Material Status Monitor: Fiber directions of the fiber-reinforced spherical shell with a slit indicated by black arrows at each spatial quadrature point. The fibers are in the direction $\mathbf{e}_z \times \mathbf{X} / \|\mathbf{X}\|$.

temperature), because the bending deformation leads to a compression of the shell wall. This is also visible at the top corner of the slit. But, the temperature is high at the left and right corner of the slit (high stretching), and on these positions of the mechanical Neumann boundary $\partial_T \mathcal{B}_0$ (narrow sides of the shell) with the highest curvature. The same also applies to the bottom. Finally, we show in bottom right plot the end position at time $t_n = 2.0$. Here, the colours indicate the dilatation $\det \mathbf{F}$ of the volume elements. Therefore, the compression zones of the bending deformations are blue coloured and the stretching zones are red coloured, except the region around the slit. The bottom buckling arises in the time interval $[1, 1.6]$, leading to suddenly increased nodal velocities.

2.2 Effects of the new strain-stress approximations

In this section, we assess the new strain-stress approximations regarding locking behaviour and computational efficiency. Note that the shell is always discretized by two elements in the thickness, independent of the chosen number of finite elements and degree of spatial shape functions.

First, we draw a comparison between the above applied D2V1F1 strain-stress approximation and the D1V0F0 space approximation with different numbers of spatial elements. In Figure 4, we show the outer boundary of the shell in the top plot, and the inner boundary of the shell in the bottom plot. Here, we indicate each space approximation by its own colour. We recognize that the blue coloured mesh with 2470 8-node/1-node hexahedral elements and D1V0F0 strain-stress approximation is comparable ‘soft’ as the D2V1F1 strain-stress approximation with 552 20-node/8-node hexahedral elements (violet mesh). Recall that the D2V1F1 space approximation introduces more nodes in the thickness of the shell than the D1V0F0 space approximations. By using less finite elements (552 elements in red and 1206 elements in green), we note a visible difference to the D2V1F1 reference solution. This is true for the bending-buckling mode of the bottom of the shell as well as the wave-shaped bending of the spherical region of the shell.

Table 2: Comparison of the top tip of the shell and the bottom tip (lowest positioned node) of the shell, calculated by the 121-scheme with 20-node/8-node (D2V1F1) and 8-node/1-node hexahedral space approximation (D1V0F0). The number behind the element indicator in the first column denotes the number n_{el} of elements.

	x_{top}	y_{top}	z_{top}	x_{bottom}	y_{bottom}	z_{bottom}	Time steps	T_{CPU}
D1V0F0 552	-1.595	-1.595	37.86	0.0000	0.0000	-16.09	674	4485
D1V0F0 1206	-1.643	-1.643	37.39	0.0000	0.0000	-17.60	661	7467
D1V0F0 2470	-1.545	-1.545	35.83	0.0000	0.0000	-18.79	663	13997
D2V1F1 552	-1.521	-1.521	35.98	0.0000	0.0000	-19.66	1184	33710

By means of the iteration status monitor¹ (ISM), we compare the numerical effort for calculating the violet mesh, the blue mesh and the green mesh by means of the number of required time steps and the CPU time per time step as well as the resulting total CPU time T_{CPU} . We summarize results of the iteration status monitor in Table 2 by numerical values. In the ISM on the left, we show the macro time step size h_n (red dots) and the number of global Newton-Raphson iterations (black dots) chosen by the iteration-count dynamic time step size control over time t_n . We recognize that the iteration numbers have constant limits, but the macro time step sizes h_n are different during the simulation. As the time steps automatically chosen with the D1V0F0 space approximations are larger than the time steps with the D2V1F1 space approximation, independent of the considered numbers of spatial elements, the total CPU time required by the D2V1F1 space approximation is clearly higher than the total CPU time of the D1V0F0 space approximations. The second reason is the higher CPU time per time step, shown in the ISM on the right (red axes). By comparing the numerical values in Table 2, we realize that the D1V0F0 space approximation with 2470 8-node/1-node hexahedral elements only requires 42% of the total CPU time of the D2V1F1 space approximation, but leads to at least 96% of the numerical results of the D2V1F1 space approximation. Note also the remarkable result that the numbers of time steps with the D1V0F0 space approximations are practically identical. Hence, we conclude that the D1V0F0 space approximation is more efficient, at least in connection with an iteration-count dynamic time step size control.

Now, by means of Figure 5, we compare the D1V0F0 space approximation (red patches) with the D1F1 space approximation (green patches) and the standard D1 space approximation (blue patches) with the same three meshes. Here, the reader get a feeling for the effect of the introduced independent strain fields \tilde{C}_F and \tilde{C}_V and the dual fields S_F and S_V on the deformation. We compare the outer boundaries of the shell in the left column, and the inner boundaries in the right column. Considering the same number of spatial elements, we clearly realize that the green meshes are more ‘flexible’ than the blue meshes, but the red meshes possess the highest flexibility. Therefore, the bending modes are reflected most accurately with independent strain fields \tilde{C}_F as well as \tilde{C}_V . For each

¹Please see each iteration status monitor (ISM) and many further plots in the lecture.

strain-stress approximation, the locking is decreasing with increasing number of spatial elements, but by comparing the red meshes in the middle and the bottom plots, we see a rather small difference. Hence, we conclude that the D1V0F0 space approximation converges remarkably ‘faster’ to the reference solution.

In the corresponding ISM’s, we also show the effort of the D1, the D1F0 and the D1V0F0 strain-stress approximation with 552, 1206 and 2470 finite elements in space. In contrast to the D1 and D1F0 space approximation, the number of time steps of the D1V0F0 strain-stress approximation is almost independent of the number of spatial elements (see Table 2). The total CPU time of each strain-stress approximation increases with the number of spatial elements, the D1V0F0 strain-stress approximation, however, runs faster than the D1 and D1F0 space approximation for each spatial mesh. The reasons are less time steps, but also a smaller CPU time per time step, because the evaluation of scalar-valued stress terms is cheaper than tensor-valued stress terms in the residuals as well as in the tangent operators (cp. Reference [12]). We realize that the D1V0F0 space approximation requires only about 74% of the standard *D1* space approximation. Hence, we conclude that the D1V0F0 space approximation remarkably improves the locking behaviour with thin-walled structures, but is also more efficient in dynamic simulations.

3 CONCLUSIONS

The combination of energy-momentum schemes with locking-free finite elements emanating from a Hu-Washizu procedure in static problems can be a difficult task. The reason is that weak forms corresponding to independent mixed fields derived by the principle of virtual work, as the dilatation \tilde{J} and the pressure p in the Simo-Taylor-Pister functional, are not associated with a continuous time curve *without* using the deformation mapping. Therefore, the deformation mapping is needed to relate the mixed fields at two successive time points of a motion. As energy-momentum schemes preserve the time evolution of energy functions, and mixed fields define these energy functions, a reliable link of energy functions to two successive time points of a motion is a fundamental precondition. But, such a continuous time curve for each independent field can be easily introduced by applying the Hu-Washizu procedure to the *principle of virtual power*. Within the framework of thermo-viscoelastic fiber-reinforced continua, we have presented a new mixed finite element formulation emanating from a mixed principle of virtual power. In this way, the *volumetric locking*, but also the *line locking* of the fibers could be reduced significantly.

On the other hand, artificial stiffening of continua discretized by locking finite elements leads to a decrease of the maximum time step size. Therefore, the presented locking-free energy-momentum schemes render larger time steps. For this reason, these energy-momentum schemes save total CPU time, and are more efficient as energy-momentum schemes with a standard (local) stress approximation. But, by applying an iteration-count dynamic time step size control only, we could show this increased computational efficiency. Hence, we have exploited their robustness with respect to time step size changes.

Acknowledgements. This research is provided by the ‘Deutsche Forschungsgemeinschaft’ (DFG) under the grant GR 3297/4-1. This support is gratefully acknowledged.

REFERENCES

- [1] Simo J.C., Taylor R.L. and Pister K.S. Variational and projection methods for the volume constraint in finite deformation elasto-plasticity. *Comput. Methods Appl. Mech. Engrg.*, 51:177–208, 1985.
- [2] Bonet J., Gil A.J. and Wood R.D. *Nonlinear solid mechanics for finite element analysis: statics*. Cambridge University Press, 2016.
- [3] Holzapfel G.A. *Nonlinear Solid Mechanics*. Wiley, Chichester, 2000.
- [4] Armero F. Assumed strain finite element methods for conserving temporal integrations in non-linear solid dynamics. *Int. J. Numer. Meth. Engrg.*, 74(12):1795–1847, 2008.
- [5] Groß M. and Dietzsch J. Variational-based energy-momentum schemes of higher-order for elastic fiber-reinforced continua. *Comput. Methods Appl. Mech. Engrg.*, 320: 509–542, 2017.
- [6] Hughes T.J.R. *The Finite Element Method*. Dover, Mineola, 2000.
- [7] Groß M., Dietzsch J. and Bartelt M. Variational-based higher-order accurate energy-momentum schemes for thermo-viscoelastic fiber-reinforced continua. *Comput. Methods Appl. Mech. Engrg.*, in press, DOI:10.1016/j.cma.2018.03.019.
- [8] Schenk O. and Gärtner K. Solving unsymmetric sparse systems of linear equations with PARDISO. *Future Generation Computer Systems*, 20(3):475–487, 2004.
- [9] Geuzaine C. and Remacle J.-F. Gmsh: A 3-D finite element mesh generator with built-in pre-and post-processing facilities. *Int. J. Numer. Methods Engrg.*, 79(11):1309–1331, 2009.
- [10] Miehe C. and Schröder J. Energy and momentum conserving elastodynamics of a non-linear brick-type mixed finite shell element. *Int. J. Numer. Meth. Engrg.*, 50(8):1801–1823, 2001.
- [11] Wriggers P. *Nichtlineare Finite-Elemente-Methoden*. Springer, 2001.
- [12] Betsch P., Janz A. and Hesch C. A mixed variational framework for the design of energy-momentum schemes inspired by the structure of polyconvex stored energy functions. *Comput. Methods Appl. Mech. Engrg.*, in press, DOI:10.1016/j.cma.2018.01.013.
- [13] Schröder B and Kuhl D. Small strain plasticity: classical versus multifield formulation. *Archive of Applied Mechanics*, 85(8):1127–1145, 2015.
- [14] Al-Kinani R. *Thermo-mechanical coupling of transversely isotropic materials using high-order finite elements*. Phd-thesis, Faculty of Mathematics/Computer Science and Mechanical Engineering, Clausthal University of Technology, 2014.

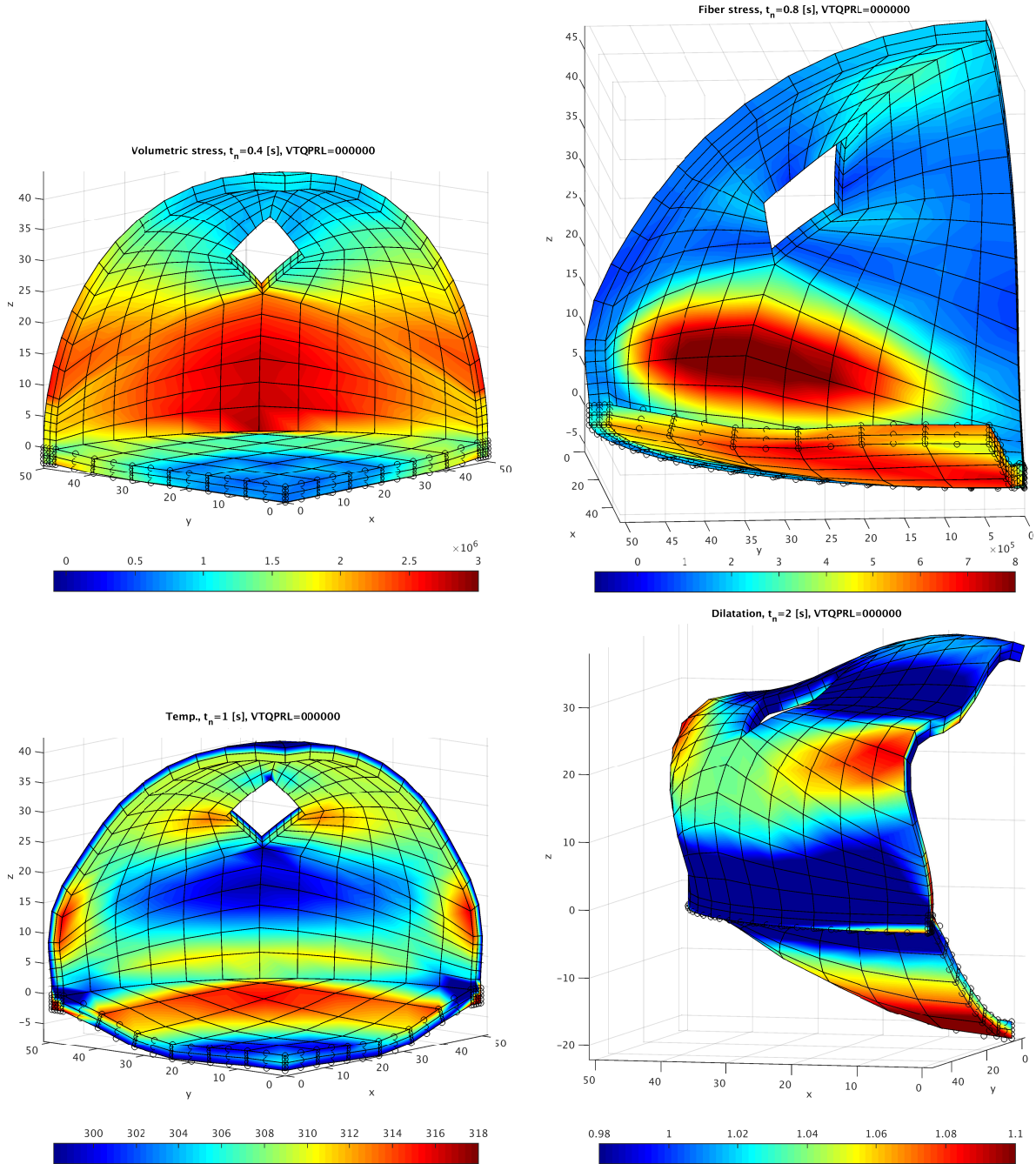


Figure 3: Motion Status Monitor: Current configurations at time $t_n = 0.4$ (top left), $t_n = 0.8$ (top right), $t_n = 1.0$ (bottom left) and $t_n = 2.0$ (bottom right). Fiber-reinforced spherical shell with a slit calculated by the 121-scheme with 552 hexahedral 20-node/8-node elements and D2V1F1 space approximation. The colours indicate the volumetric stress S_V (top left), the fiber stress S_F (top right), the body temperature Θ (bottom left) and the dilatation $\det \mathbf{F}$ of the volume elements, respectively. No vector informations are displayed (VTQPRL=000000).

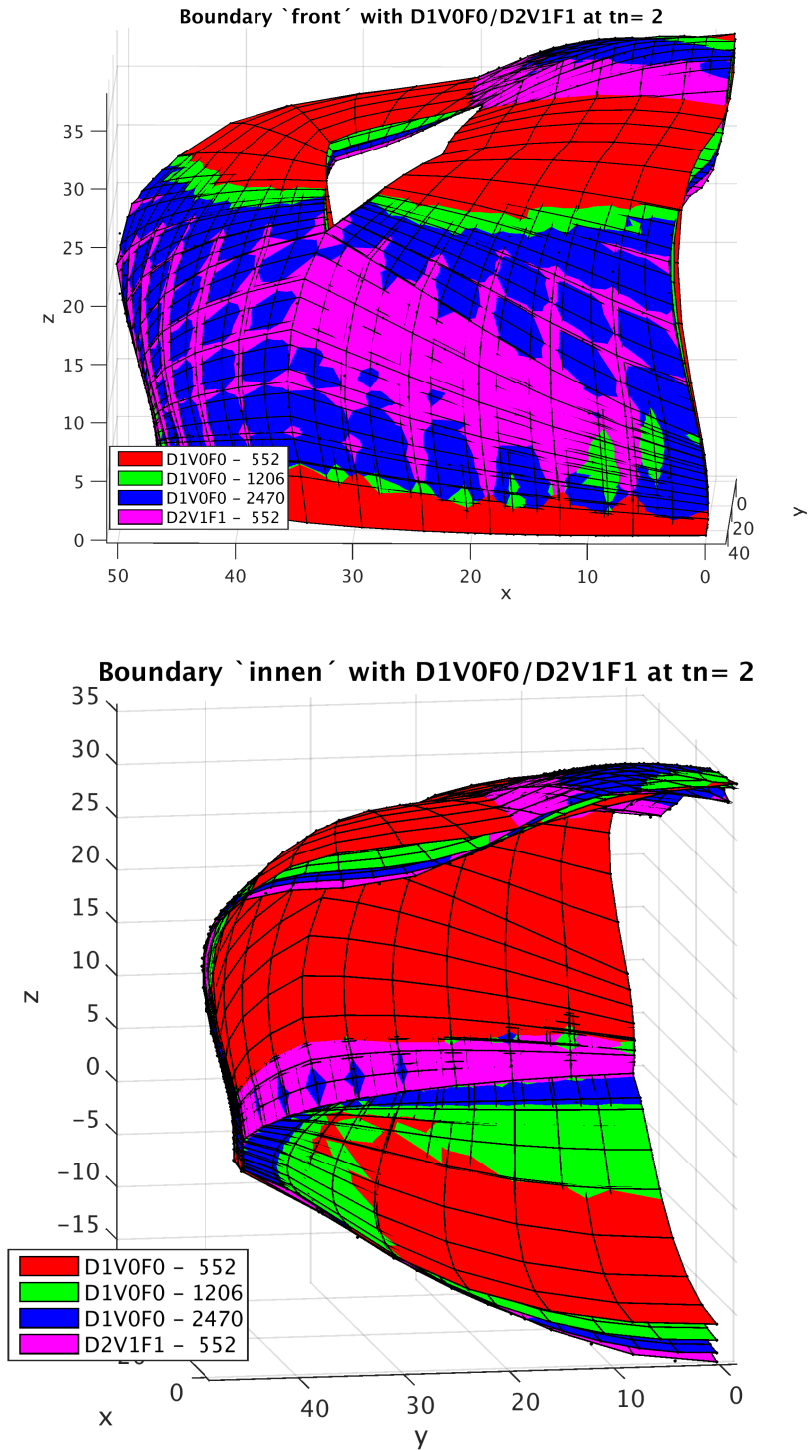


Figure 4: Sections of the fiber-reinforced spherical shell with a slit at time $t_n = 2.0$, calculated by the 121-scheme with different space approximations. Colours indicate the different stress approximations and the number behind the minus sign in the legend denotes the number of elements. View on the outer (top plot) and inner (bottom plot) boundary of the shell.

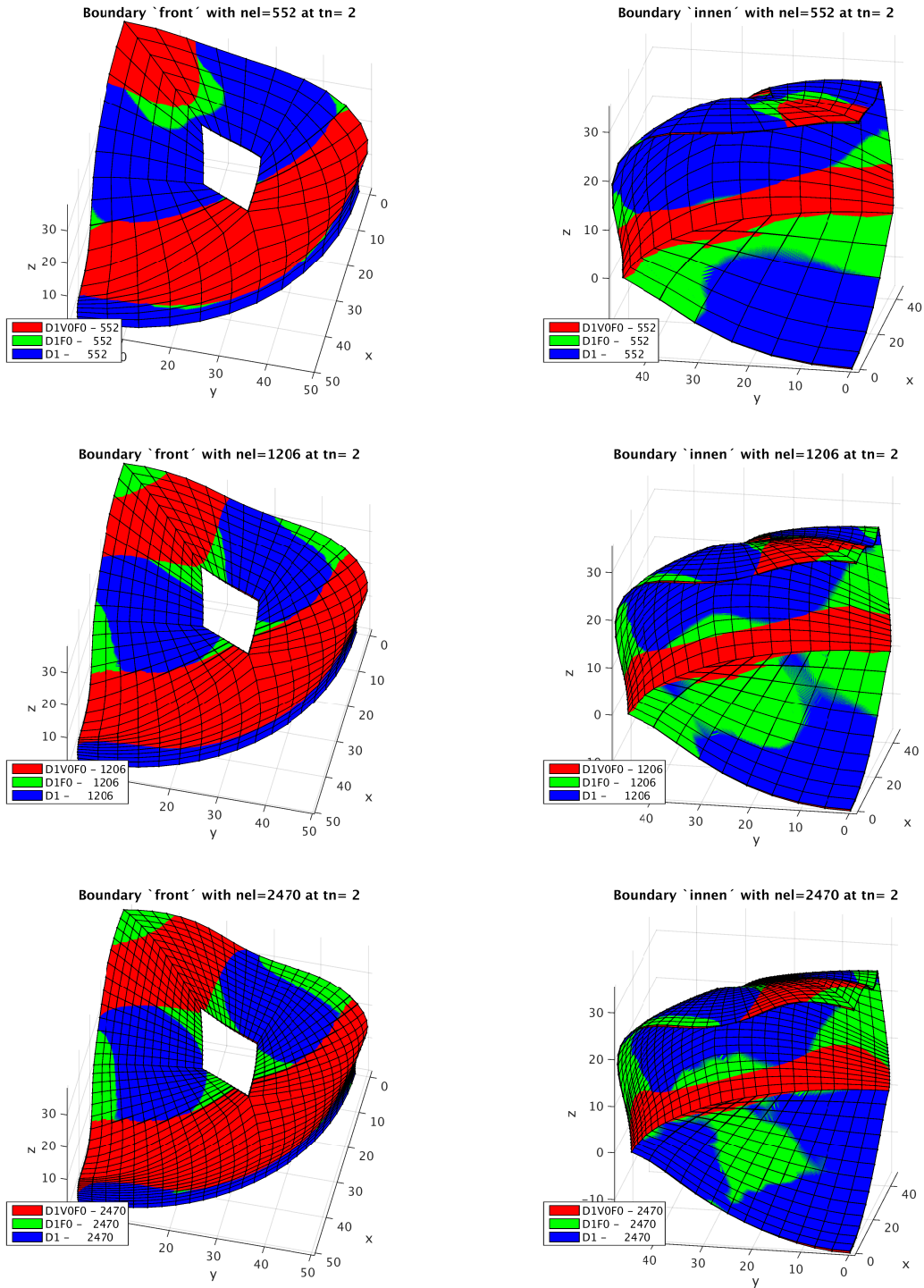


Figure 5: Sections of the fiber-reinforced spherical shell with a slit at time $t_n = 2.0$, calculated by the 121-scheme with different strain-stress approximations. Colours indicate the different space approximations. View on the outer (left plots) and inner (right plots) boundary of the shell.